AGU PUBLICATIONS

Geophysical Research Letters

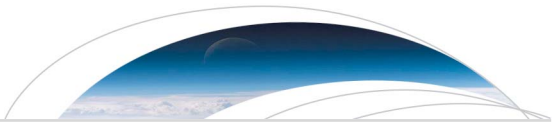

RESEARCH LETTER

10.1002/2014GL062273

Key Points:
- Quantitative analysis of the first balloon REP with closely conjugate EMIC waves
- Our simulation suggests EMIC waves to be a viable cause for the REP event
- The adopted model is proved to be applicable to simulating the REP event

Correspondence to:
Z. Li,
Zan.Li.GR@dartmouth.edu

Citation:
Li, Z., et al. (2014), Investigation of EMIC wave scattering as the cause for the BARREL 17 January 2013 relativistic electron precipitation event: A quantitative comparison of simulation with observations, *Geophys. Res. Lett.*, *41*, 8722–8729, doi:10.1002/2014GL062273.

Received 21 OCT 2014
Accepted 5 DEC 2014
Accepted article online 10 DEC 2014
Published online 23 DEC 2014

Investigation of EMIC wave scattering as the cause for the BARREL 17 January 2013 relativistic electron precipitation event: A quantitative comparison of simulation with observations

Zan Li[1], Robyn M. Millan[1], Mary K. Hudson[1], Leslie A. Woodger[1], David M. Smith[2], Yue Chen[3], Reiner Friedel[3], Juan V. Rodriguez[4], Mark J. Engebretson[5], Jerry Goldstein[6], Joseph F. Fennell[7], and Harlan E. Spence[8]

[1]Department of Physics and Astronomy, Dartmouth College, Hanover, New Hampshire, USA, [2]Physics Department and Santa Cruz Institute for Particle Physics, University of California, Santa Cruz, California, USA, [3]Los Alamos National Laboratory, Los Alamos, New Mexico, USA, [4]Cooperative Institute for Research in Environmental Sciences, University of Colorado Boulder, Boulder, Colorado, USA, [5]Department of Physics, Augsburg College, Minneapolis, Minnesota, USA, [6]Southwest Research Institute, San Antonio, Texas, USA, [7]Space Science Applications Laboratory, Aerospace Corporation, Los Angeles, California, USA, [8]Institute for the Study of Earth, Oceans, and Space, University of New Hampshire, Durham, New Hampshire, USA

Abstract Electromagnetic ion cyclotron (EMIC) waves were observed at multiple observatory locations for several hours on 17 January 2013. During the wave activity period, a duskside relativistic electron precipitation (REP) event was observed by one of the Balloon Array for Radiation belt Relativistic Electron Losses (BARREL) balloons and was magnetically mapped close to Geostationary Operational Environmental Satellite (GOES) 13. We simulate the relativistic electron pitch angle diffusion caused by gyroresonant interactions with EMIC waves using wave and particle data measured by multiple instruments on board GOES 13 and the Van Allen Probes. We show that the count rate, the energy distribution, and the time variation of the simulated precipitation all agree very well with the balloon observations, suggesting that EMIC wave scattering was likely the cause for the precipitation event. The event reported here is the first balloon REP event with closely conjugate EMIC wave observations, and our study employs the most detailed quantitative analysis on the link of EMIC waves with observed REP to date.

1. Introduction

Electromagnetic ion cyclotron (EMIC) waves have been proposed as a mechanism to rapidly scatter relativistic electrons into the loss cone through Doppler-shifted resonant interactions [*Albert*, 2003; *Summers and Thorne*, 2003; *Thorne et al.*, 2006]. The interactions are expected to be the most effective in the dusk sector [*Thorne and Kennel*, 1971; *Albert*, 2003; *Summers and Thorne*, 2003] and are often associated with simultaneous ion precipitation caused by gyroresonance between ions and EMIC waves [*Thorne and Andreoli*, 1981]. Many observations support the link between relativistic electron precipitation (REP) and EMIC waves. The preferential occurrence of REP on the duskside has been observed by both satellites [*Vampola*, 1971; *Green et al.*, 2004; *Carson et al.*, 2013; *Comess et al.*, 2013] and balloons [*Foat et al.*, 1998; *Lorentzen et al.*, 2000; *Millan et al.*, 2002]. Coincident precipitation of electrons and ions has been reported by various satellite studies [*Imhof et al.*, 1986; *Bortnik et al.*, 2006; *Sandanger et al.*, 2009; *Carson et al.*, 2013].

Simultaneous observations of EMIC waves and REP, however, are uncommon. *Engebretson et al.* [2008] and *Rodger et al.* [2008] reported several REP events with strong riometer absorption and subionospheric VLF propagation, respectively, and simultaneous EMIC wave activities observed by ground magnetometers. *Miyoshi et al.* [2008] reported coincident ion and electron precipitation observed by one of the Polar-orbiting Operational Environmental Satellites (POES) into a proton aurora in conjunction with ground magnetometer EMIC wave observations. All of these observations showed correlation but could not provide a quantitative analysis to test the theory. Strong observational evidence that can be used to quantify the EMIC wave-driven REP is still lacking. The Balloon Array for Radiation belt Relativistic Electron Losses (BARREL) campaign, conducted in the 2013 and 2014 Austral summer seasons during the Radiation Belt

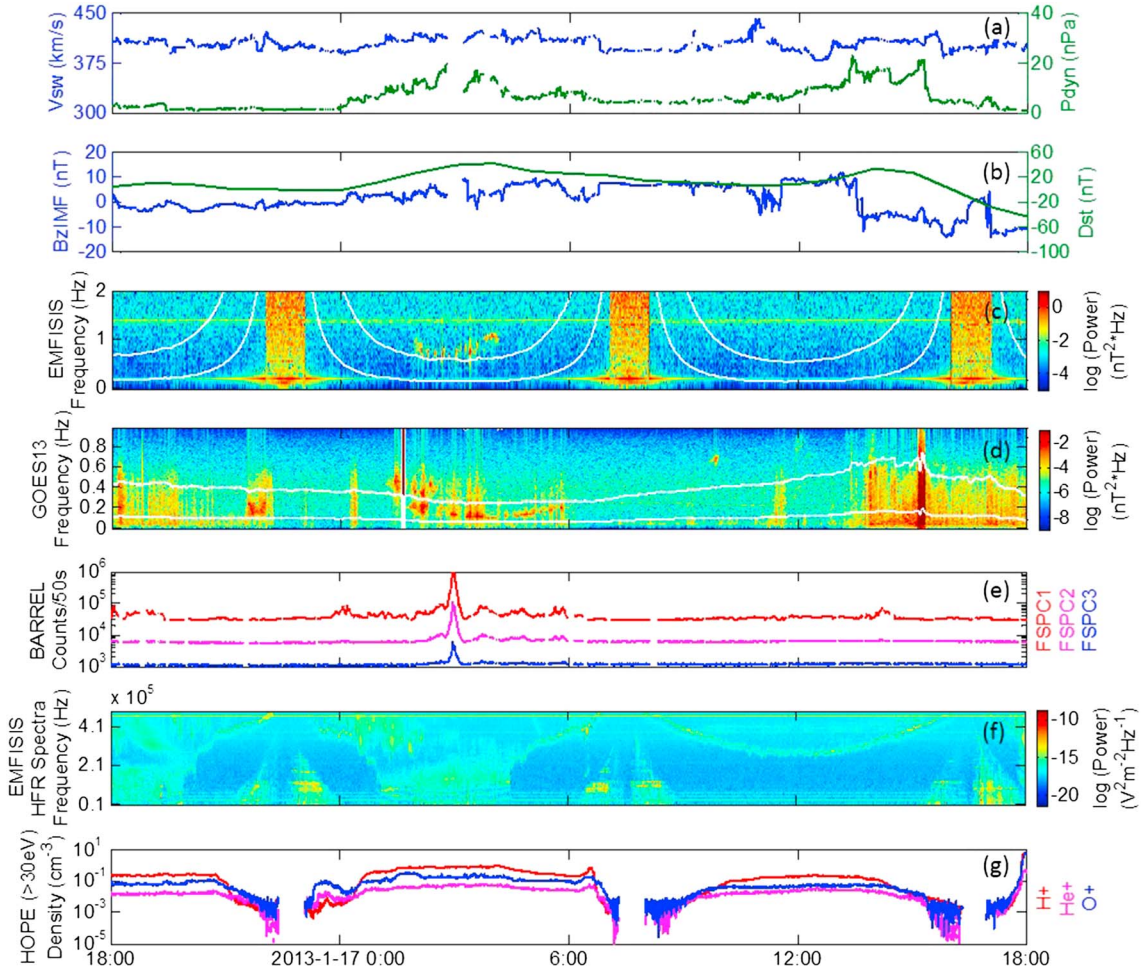

Figure 1. (a) OMNI solar wind speed and dynamic pressure. (b) OMNI *Bz* of IMF (in GSM) and *Dst*. (c and d) EMIC waves measured by RBSP EMFISIS-A and GOES 13 magnetometers. The white lines are O^+ and He^+ gyrofrequencies. (e) X-ray fast spectrum measured by BARREL balloon 1G (FSPC1: <180 keV, FSPC2: 180–550 keV, FSPC3: 550–840 keV). (f) Upper hybrid resonance frequency in the HFR spectrum measured by RBSP EMFISIS-A. (g) >30 eV ion density observed by RBSP-ECT HOPE-A.

Storm Probes (RBSP, now called "the Van Allen Probes") mission, provides the first balloon measurements of REP while comprehensive in situ measurements of both plasma waves and energetic particles are available [*Millan et al.*, 2013].

In the present paper we analyze a REP event observed by BARREL during a period of strong EMIC wave activity. The event was in close conjunction with EMIC waves observed by Geostationary Operational Environmental Satellite (GOES) 13. The energy distribution of REP caused by scattering with EMIC waves is simulated using parameters provided by GOES 13 and the Van Allen Probes and is compared with BARREL spectrometer data. The event reported in this paper is the first balloon REP event with closely conjugate EMIC wave observations, and the presented study is by far the most detailed quantitative analysis on the link of EMIC waves with observed REP.

2. Observations

The REP event reported here occured on 17 January 2013, which was moderately active day, *Kp* around 2 to 4 (not shown). A moderate storm sudden commencement occurred at around 0 UT in association with an increase in solar wind dynamic pressure, followed by a geomagnetic storm, with *Dst* reaching ~−60 nT at the end of the day (Figures 1a and 1b). Between 01 and 06 UT, long-lasting EMIC waves were observed from ground and space throughout the duskside/nightside magnetosphere, ranging over *L*~4.5–8 and MLT~15:40–03:30. The instruments that detected the waves include GOES 13 and 15, the Van Allen Probes, the Canadian Array for Realtime Investigations of Magnetic Activity ground magnetometer in Dawson City,

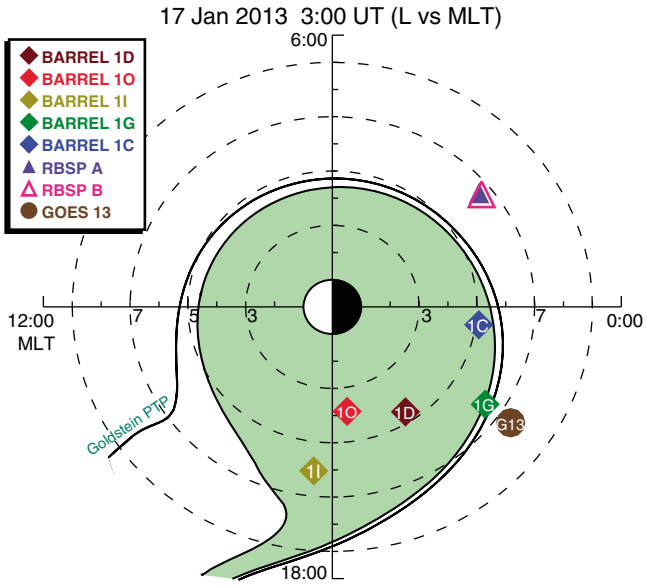

Figure 2. Magnetic (T89) equatorial locations of spacecraft, balloons, and the plasmapause simulated by the plasmapause test particle (PTP) model.

Canada, and the British Antarctic Survey (BAS) ground magnetometer at Halley, Antarctica [*Weaver et al.*, 2013]. While ground observations cannot determine the wave band due to horizontal ducting, the EMIC waves observed by the Van Allen Probes (e.g., Figure 1c for Van Allen Probes A) and the GOES satellites (e.g., Figure 1d for GOES 13) were in the hydrogen and the helium band, respectively. During this period, three relativistic electron precipitation events were observed by BARREL balloon 1G, 1C, and 1I at different times. Mapped to the magnetic equator using the International Radiation Belt Environment Modeling Library (IRBEM-LIB, formerly the ONERA-DESP library) in the magnetic field model of *Tsyganenko* [1989] (T89), the 03 UT event observed by balloon 1G was found to be at MLT∼22 h and L∼6.5 (Figure 2), in close conjunction with the EMIC waves observed by GOES 13 (MLT∼22 h and L∼7.5; cf. Figures 1d and 2), suggesting the waves may have scattered the electrons into the loss cone. This precipitation event observed by 1G lasted for about 20 min from ∼02:48:20–03:08:20 UT (Figure 1e).

We focus on this conjunction event in the present study. We solve the Fokker-Planck pitch angle diffusion equation using the diffusion coefficient derived by *Summers and Thorne* [2003] and *Summers et al.* [2007] in order to simulate the evolution of the distribution of electrons due to scattering with EMIC waves and to compute the precipitating electron flux at the boundary of the atmosphere. Details about the model can be found in *Li et al.* [2013], and the simulation results are shown in the next section. Items 1 through 6 directly below list the input parameters of the model that we obtained from GOES 13 and the Van Allen Probes observations:

1. Initial trapped electron population: When the precipitation event occurred at 03 UT, the 30 keV–600 keV Magnetospheric Electron Detector (MAGED) [*Hartley et al.*, 2013] of GOES 13 observed a "butterfly" electron pitch angle distribution (PAD), a typical PAD on the nightside at GEO caused by the drift shell splitting effect [*West et al.*, 1973; *Baker et al.*, 1978; *Chen et al.*, 2014]. To estimate the flux of higher-energy electrons, we assume they have the same PAD as the particles observed by the highest energy channel (350–600 keV) of MAGED and calculate their energy differential flux from the integral flux measured by the E1 (>0.8 MeV) and E2 (>2 MeV) channels of the Energetic Proton Electron and Alpha Detector (EPEAD) [*Rodriguez et al.*, 2010] of GOES 13 using the method derived by *Onsager et al.* [2004] and *Gannon et al.* [2012], which assumes a relativistic Maxwellian interpolation. Figure 3a shows the <600 keV PAD observed by GOES 13 and the >600 keV PAD calculated using this method.

   The Van Allen Probes were at their apogees (L∼6.5, MLT∼2.6) at 03 UT. Probes A and B observed very similar features, due to the proximity of the two spacecraft during this day. We analyze the electron flux measurements from the Relativistic Electron Proton Telescope (REPT) [*Baker et al.*, 2013] and the Magnetic Electron Ion Spectrometer (MagEIS) [*Blake et al.*, 2013] of the Energetic Particle, Composition, and Thermal Plasma suite [*Spence et al.*, 2013]. Since the calibration efforts on REPT remain ongoing, we use a simple linear adjustment factor in the instrument overlap region to match the flux observed by REPT with MagEIS and plot in Figure 3a both electron fluxes as a function of pitch angle. Although PAD generally varies with MLT, the Van Allen Probes and GOES 13 observed a similar PAD, due to the fact that they were symmetrically located about the noon-midnight meridian plane, where the drift shell splitting effects are often similar. The flux level observed by the Van Allen Probes, however, was higher than GOES 13 by less than an order of magnitude (Figure 3a. Note the differences between instrument energy channels.),

likely because the probes were at a lower L. The energy distribution (e.g., Figure 3b for 90° pitch angle) observed by the Van Allen Probes followed a broken power law distribution [*Mauk and Fox*, 2010] with a break at ~1.6 MeV. Considering the better energy and angular resolution than GOES 13 as well as the similarity in L with balloon 1G, we use the trapped flux measured by the Van Allen Probes in our simulation. We fit a broken power law to the electron energy distribution using equation (7) in *Mauk and Fox* [2010] with fitting parameters $C = 9 \times 10^{13}$, $kT = 20$, $\gamma_1 = 4$, $E_0 = 1600$, and $\gamma_2 = 6.5$, and Legendre polynomials to the unbinned electron pitch angle data using equation (1) in *Chen et al.* [2014] with normalized coefficients 0.013, −0.35, 0.0024, and −0.4 for first–fourth orders and zero for higher orders. The flux near the loss cone is extrapolated from the Legendre polynomial fit.

2. Wave power distribution: Although EMIC waves were observed at many different locations, we use the wave properties measured by GOES 13, because when mapped to the magnetic equator, it was the closest to the balloon. The waves observed by the magnetometer of GOES 13 lasted from ~02:52:00–03:12:00 UT, lagging behind the REP event by a little less than 4 min, likely because GOES 13 entered the rotating plasmapause at a later time than balloon 1G ([*Goldstein et al.*, 2014], cf. Figure 2 in the present paper), and the high density plasmasphere has been suggested to be a preferable region for EMIC wave occurrence [*Horne and Thorne*, 1993; *Spasojević et al.*, 2004; *Yahnin and Yahnina*, 2007; *Chen et al.*, 2010; *Usanova et al.*, 2013]. The wave amplitude was modulated by ULF waves and fluctuated between ~0–1 nT (plot above Figure 4d). The wave frequency spectrum is fit by a Gaussian with maximum frequency ω_m ~0.147 Hz, and half width $\delta\omega$~0.02 Hz. We use the corresponding frequency ratios $\omega_m/\Omega_{O+} = 2.25$ and $\delta\omega/\Omega_{O+} = 0.31$ in our simulation, because between the L values of balloon 1G and GOES 13, the wave frequency ratios have been proposed to be roughly constant, assuming constant cold ion composition [*Denton et al.*, 2014]. In addition, although theoretically, the wave frequency to be considered in the diffusion coefficient calculations should range from 0 to infinity [*Lyons et al.*, 1971], for computational convenience, we only integrate the waves within the helium band, with a lower cutoff at the boundary of the stop band above O^+ gyrofrequency and a higher cutoff at the He^+ gyrofrequency. This is justified because the wave power in the oxygen and hydrogen bands was negligible.
3. Cold plasma density: Since the wave power is centered well below the He^+ gyrofrequency, the finite beta effect is ignorable [*Chen et al.*, 2011, 2013] and the cold wave dispersion relation is used in computing the diffusion coefficient. Since GOES 13 does not provide plasma density observations, we calculate the plasma density using the upper hybrid resonance (UHR) frequency provided by the Electric and Magnetic Field Instrument and Integrated Science (EMFISIS) [*Kletzing et al.*, 2013] on the Van Allen Probes. At 03 UT, balloon 1G was shown by a plasmapause test particle (PTP) model [*Goldstein et al.*, 2014] to be at the main plasmapause wrapped inside a residual plume (Figure 2). At the same time, as suggested by both EMFISIS UHR frequency observations (Figure 1f) and the PTP model [*Goldstein et al.*, 2014], the Van Allen Probes were outside the plasmasphere, where the plasma density could be very different from the wave region. However, as the plasmapause rotated eastward [*Goldstein et al.*, 2014], when the spacecraft came back to their apogees (with an L value similar to the REP event) at 12 UT, the spacecraft was inside the plasmasphere, as indicated by the EMFISIS UHR frequency observations (Figure 1f). We then use the UHR frequency measured at 12 UT to calculate the plasma density, which is determined to be 100 cm^{-3}. Meanwhile, the Helium Oxygen Proton Electron (HOPE) sensor [*Funsten et al.*, 2013] on the Van Allen Probes observed that the warm/hot (>30 eV) component of the ion density was 0.27 cm^{-3} (Figure 1g). Assuming charge neutrality, this warm/hot plasma component is negligible compared to the total density 100 cm^{-3}.
4. Cold ion composition: Since HOPE only provides warm/hot (>30 eV) ion densities, we use other methods to determine the cold ion composition. At 12 UT, Alfven wave activity was seen by EMFISIS and the Electric Fields and Waves (EFW) instrument [*Wygant et al.*, 2013] on the Van Allen Probes. From the observed third Alfven harmonic frequency (12.5 mHz), we obtain the total mass density 121 amu/cm^3 (R. E. Denton and K. Takahashi, private communication, 2014). In comparison, by adding up the H^+, He^+, and O^+ mass densities observed by HOPE (Figure 1g), we find that the >30 eV ion mass density is 1 amu/cm^3, a negligible fraction of the total mass density. Assuming charge neutrality and the ratio of cold $He^+ : H^+ = 4.4\%$ [*Farrugia et al.*, 1989], we solve the mass density equation [*Takahashi et al.*, 2008, equation (8)] with the cold number density 100 cm^{-3} and obtain the density ratios $H^+ : He^+ : O^+ = 95.3 : 4.2 : 0.5$. This estimate is very similar to many statistical study results [*Chappell et al.*, 1970; *Young et al.*, 1977; *Horwitz et al.*, 1981].

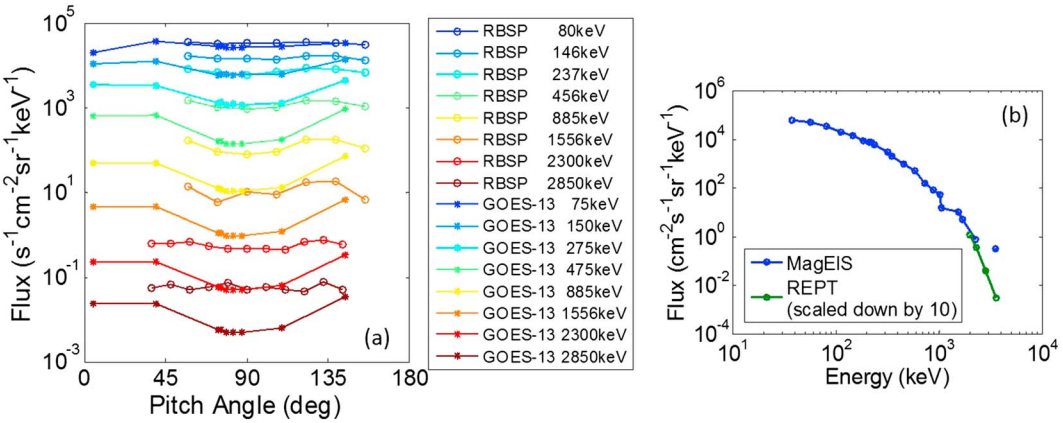

Figure 3. (a) Electron pitch angle distribution from RBSP-ECT MagEIS-A and REPT-A (binned) and GOES 13 MAGED and EPEAD. (b) Electron energy distribution of 90° pitch angles from RBSP-ECT MagEIS-A and REPT-A.

5. Background magnetic field: Tracing from balloon 1G using IRBEM-LIB in T89, we estimate the minimum magnetic field near the magnetic equator conjugate to the balloon to be 41.1 nT; we use this value as the equatorial background magnetic field in our simulation.
6. Wave-particle interaction spatial scale: Since GOES 13 detected EMIC waves when it traversed a 20 min MLT span during the event, we determine the interaction region to be 1.4% of the drift orbit. Although EMIC waves were observed over a broader region, we do not use a higher percentage because the plasma conditions at other locations were different and we do not find them favorable for the wave-particle resonant interaction. This is supported by the fact that, at this time, REP was not observed by any other BARREL balloon or any other Polar-orbiting Operational Environmental Satellite (POES) than N19, which was in close conjunction with 1G ([*Weaver et al.*, 2013], as well as S. Shekhar, private communication, 2014). We further assume the interaction region to be within ±15° in magnetic latitude, where the waves are believed to be mostly field aligned with left-hand circular polarization and can most strongly scatter electrons [*Albert*, 2003; *Loto'aniu et al.*, 2005; *Hu and Denton*, 2009].

3. Simulations

We use the diffusion model described in *Li et al.* [2013] to simulate the time evolution of the energy distribution of the REP flux during the 20 min precipitation event. The simulation parameters used are those described in the previous section. The diffusion coefficient is plotted in Figure 4a. The simulated precipitation is found to be the strongest near 1.2 MeV and falls sharply at lower and higher energies (Figure 4b). We then use the BARREL standard response model ([*Millan et al.*, 2013]) to determine the bremsstrahlung X-rays that would be detected by the balloon-borne scintillator given the simulated incident precipitating electrons at the boundary of the atmosphere. The BARREL standard response model is derived from GEANT-3 Monte Carlo simulations that include all relevant particle interactions such as ionization losses of precipitating electrons, bremsstrahlung production, and scattering of X-rays in the atmosphere and BARREL instruments. We acquire the X-ray backgrounds before and after the precipitation event and compare the background subtracted X-ray medium spectrum observed by BARREL balloon 1G with the simulated X-rays. The simulated count rate is shown to be very close to that observed, only 2.7 times higher on average, and 3.5 times higher at the strongest precipitation peak. We show the comparisons in Figures 4d and 4e, where we divide the simulated flux level by 3.5 and average the count rates within every 8 s to show the details of the temporal structure (The time resolution of the BARREL medium spectrum is 4 s.). The black lines are the total X-ray count rates integrated over energy at every time step (The simulated total count rate is divided by 3.5.). Although the counting statistics in the observed spectrum (Figure 4e), especially at high energies, is affected by using a small 8 s time step, the variation of the observed count rate is reproduced in the simulated count rate (Figure 4d). Shown above Figure 4d is the time variation of the EMIC wave amplitude observed by GOES 13. The ULF modulation frequency, as well as the growth and decay time of the EMIC waves are reflected in REP. Shown in Figure 4c as an example is a line plot of the energy distribution of the X-ray count rates averaged between the two strongest peaks in the middle of the event (02:57:30–02:59:30 UT). We can see that the simulated energy distribution of the X-rays (black solid

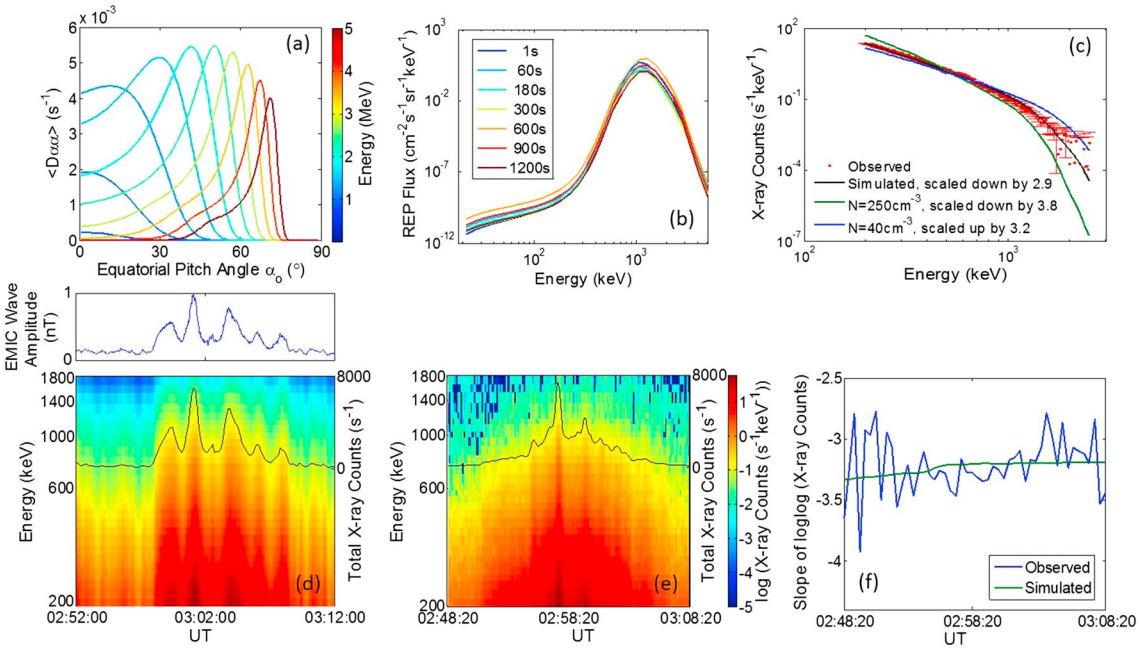

Figure 4. (a) Bounce- and drift-averaged pitch angle diffusion coefficients for EMIC waves interacting with electrons. (b) Time variation of the energy distribution of the simulated precipitating electrons. (c) Log-log line plot of the energy distribution of the bremsstrahlung X-ray count rate averaged over 02:57:30–02:59:30 UT from the medium spectrum of BARREL balloon 1G (with error bars, background subtracted), the simulation with estimated parameters, and two test simulations with densities changed to 40 cm^{-3} and 250 cm^{-3}. (d and e) Time variation of the bremsstrahlung X-rays from simulation and balloon 1G medium spectrum (background subtracted). The black lines are the total X-ray count rates integrated over energy at every time step. The simulated count rate has been divided by 3.5. Above Figure 4d is the time variation of the EMIC wave amplitude observed by GOES 13. (f) Time variation of the slope of the linear fit on [400, 800] keV of the log-log line plot of the simulated and observed (background subtracted) bremsstrahlung X-ray energy spectrum.

curve) matches that observed (red dotted curve) very well (other curves in the plot are discussed in the next section). We then apply a linear fit in the energy interval [400, 800] keV on the log-log line plot at every 24 s and characterize the evolution of the hardness of the spectrum using the slope of the linear fit. Shown in Figure 4f, the hardness of the simulated and the observed spectra are very similar, both becoming slightly harder with time.

However, there are a few differences between the simulated and observed X-ray spectra. First, though very similar, the simulated flux is still higher than the observed by 2.7 times on average. Second, the time variation of the observed X-ray count rate (Figure 4e) is more gradual than the simulated count rate (Figure 4d). Especially before the first peak (~02:54 UT), when the observed EMIC wave amplitude was small and constant, the simulated precipitation does not show an evident gradual increase as that in the observed spectrum. These differences are likely due to the slightly different wave profiles at GOES 13 and the diffusion region, because the satellite and the balloon were not perfectly conjugate. The difference in the flux levels may also be a result of the different trapped flux levels at the Van Allen Probes and the diffusion region. Furthermore, please note that the BARREL standard response matrix assumes a downward isotropic REP flux distribution, corresponding to a flat loss cone distribution that resulted from highly strong diffusion. If we instead assume that the loss cone flux increases with pitch angle, which was what happened in this event according to our diffusion simulation, fewer bremsstrahlung X-rays will arrive at the balloon altitude and the simulated X-ray count rate will be lower. According to our test simulation, a mirroring REP flux distribution of pitch angles between 80 and 90° reduces the expected X-ray count rate by a factor of ~2 over a downward isotropic REP flux distribution and hence causes the expected X-ray count rate to be closer to what was observed.

4. Summary and Discussion

This paper analyzes a relativistic electron precipitation event observed by BARREL during a period of strong EMIC wave activity. We simulated the electron pitch angle diffusion using wave and particle parameters observed by GOES 13 and Van Allen probes and compared results with balloon observations. We showed

that the simulated precipitation reproduced the balloon observations to a large degree in count rate, energy distribution, and the temporal variation, indicating that EMIC wave scattering was a likely cause for the precipitation event, and the adopted diffusion model did a good job simulating the wave-particle interactions during the event. Reported here is the first balloon REP event with closely conjugate EMIC wave observations, and our study adopts the most detailed quantitative analysis on the link of EMIC waves with observed REP to date.

Since the REP flux and energy distribution strongly depends on the wave, particle, and plasma parameters [*Li et al.*, 2013], and our bremsstrahlung X-ray response model proves to be very sensitive to the variations in REP caused by changes in the input parameters of the diffusion model, the X-ray spectrum simulated by our model can be used to effectively test the conditions of the precipitation caused by EMIC wave scattering. Higher initial trapped flux, stronger waves, and broader interaction spatial coverage will cause the REP flux to increase and hence result in a higher X-ray count rate, and vice versa; weaker equatorial background magnetic field, higher wave frequency, and greater cold plasma density will not only cause the REP flux level to increase but also lower the energy of the peak in the REP energy spectrum, leading to a higher count rate as well as a softer X-ray energy spectrum, and vice versa [*Li et al.*, 2013] (Shown in Figure 4c are two test simulations with cold plasma density increased and decreased by a factor of 2.5.). The presented approach of comparing the X-ray spectra should be further exploited in testing the role of EMIC waves in relativistic electron precipitation.

Acknowledgments

The BARREL campaigns were supported by NASA grant NNX08AM58G, the National Environmental Research Council (NERC), British Antarctic Survey (BAS), and the South African National Antarctic Program (SANAP). Additional work at Dartmouth was supported by NASA grant NNX13AD65G, ECT (967399) subcontract from UNH, EFW (922613) subcontract from UMN, and by JHU/APL under NASA prime contract NAS5-01072. Juan V. Rodriguez was supported by NASA LWS TR&T Interagency Purchase Request NNH13AV99I to the National Geophysical Data Center. Work at Augsburg College was supported by NSF grant PLR-1341493. Modeling work by Jerry Goldstein was supported by the NASA Van Allen Probes missions RBSP-ECT project, the NASA Heliophysics Guest Investigator program under NNX07AG48G, and the NSF Geospace Environment Modeling program under ATM0902591. The Aerospace efforts are supported by a JHU/APL Van Allen Probes contract 967399. We would also like to thank the Van Allen Probes, GOES and BARREL teams for data and many helpful discussions.

The Editor thanks Kazo Shiokawa and an anonymous reviewer for their assistance in evaluating this paper.

References

Albert, J. M. (2003), Evaluation of quasi-linear diffusion coefficients for EMIC waves in a multispecies plasma, *J. Geophys. Res.*, *108*(A6), 1249, doi:10.1029/2002JA009792.

Baker, D., et al. (2013), The Relativistic Electron-Proton Telescope (REPT) instrument on board the Radiation Belt Storm Probes (RBSP) spacecraft: Characterization of Earth's radiation belt high-energy particle populations, *Space Sci. Rev.*, *179*(1-4), 337–381, doi:10.1007/s11214-012-9950-9.

Baker, D. N., P. R. Higbie, E. W. Hones, and R. D. Belian (1978), High-resolution energetic particle measurements at 6.6 R_E 3. Low-energy electron anisotropies and short-term substorm predictions, *J. Geophys. Res.*, *83*(A10), 4863–4868, doi:10.1029/JA083iA10p04863.

Blake, J., et al. (2013), The Magnetic Electron Ion Spectrometer (MagEIS) instruments aboard the Radiation Belt Storm Probes (RBSP) spacecraft, *Space Sci. Rev.*, *179*(1-4), 383–421, doi:10.1007/s11214-013-9991-8.

Bortnik, J., R. M. Thorne, T. P. O'Brien, J. C. Green, R. J. Strangeway, Y. Y. Shprits, and D. N. Baker (2006), Observation of two distinct, rapid loss mechanisms during the 20 November 2003 radiation belt dropout event, *J. Geophys. Res.*, *111*, A12216, doi:10.1029/2006JA011802.

Carson, B. R., C. J. Rodger, and M. A. Clilverd (2013), POES satellite observations of EMIC-wave driven relativistic electron precipitation during 1998–2010, *J. Geophys. Res. Space Physics*, *118*, 232–243, doi:10.1029/2012JA017998.

Chappell, C. R., K. K. Harris, and G. W. Sharp (1970), A study of the influence of magnetic activity on the location of the plasmapause as measured by OGO 5, *J. Geophys. Res.*, *75*(1), 50–56, doi:10.1029/JA075i001p00050.

Chen, L., R. M. Thorne, V. K. Jordanova, C.-P. Wang, M. Gkioulidou, L. Lyons, and R. B. Horne (2010), Global simulation of EMIC wave excitation during the 21 April 2001 storm from coupled RCM-RAM-HOTRAY modeling, *J. Geophys. Res.*, *115*, A07209, doi:10.1029/2009JA015075.

Chen, L., R. M. Thorne, and J. Bortnik (2011), The controlling effect of ion temperature on EMIC wave excitation and scattering, *Geophys. Res. Lett.*, *38*, L16109, doi:10.1029/2011GL048653.

Chen, L., R. M. Thorne, Y. Shprits, and B. Ni (2013), An improved dispersion relation for parallel propagating electromagnetic waves in warm plasmas: Application to electron scattering, *J. Geophys. Res. Space Physics*, *118*, 2185–2195, doi:10.1002/jgra.50260.

Chen, Y., R. H. W. Friedel, M. G. Henderson, S. G. Claudepierre, S. K. Morley, and H. E. Spence (2014), REPAD: An empirical model of pitch angle distributions for energetic electrons in the Earth's outer radiation belt, *J. Geophys. Res. Space Physics*, *119*, 1693–1708, doi:10.1002/2013JA019431.

Comess, M. D., D. M. Smith, R. S. Selesnick, R. M. Millan, and J. G. Sample (2013), Duskside relativistic electron precipitation as measured by SAMPEX: A statistical survey, *J. Geophys. Res. Space Physics*, *118*, 5050–5058, doi:10.1002/jgra.50481.

Denton, R. E., V. K. Jordanova, and B. J. Fraser (2014), Effect of spatial density variation and O^+ concentration on the growth and evolution of electromagnetic ion cyclotron waves, *J. Geophys. Res. Space Physics*, *119*, 8372–8395, doi:10.1002/2014JA020384.

Engebretson, M. J., et al. (2008), Pc1–Pc2 waves and energetic particle precipitation during and after magnetic storms: Superposed epoch analysis and case studies, *J. Geophys. Res.*, *113*, A01211, doi:10.1029/2007JA012362.

Farrugia, C. J., D. T. Young, J. Geiss, and H. Balsiger (1989), The composition, temperature, and density structure of cold ions in the quiet terrestrial plasmasphere: GEOS 1 results, *J. Geophys. Res.*, *94*(A9), 11,865–11,891, doi:10.1029/JA094iA09p11865.

Foat, J. E., R. P. Lin, D. M. Smith, F. Fenrich, R. Millan, I. Roth, K. R. Lorentzen, M. P. McCarthy, G. K. Parks, and J. P. Treilhou (1998), First detection of a terrestrial MeV X-ray burst, *Geophys. Res. Lett.*, *25*(22), 4109–4112, doi:10.1029/1998GL900134.

Funsten, H., et al. (2013), Helium, Oxygen, Proton, and Electron (HOPE) mass spectrometer for the Radiation Belt Storm Probes mission, *Space Sci. Rev.*, *179*(1-4), 423–484, doi:10.1007/s11214-013-9968-7.

Gannon, J. L., S. R. Elkington, and T. G. Onsager (2012), Uncovering the nonadiabatic response of geosynchronous electrons to geomagnetic disturbance, *J. Geophys. Res.*, *117*, A10215, doi:10.1029/2012JA017543.

Goldstein, J., S. D. Pascuale, C. Kletzing, W. Kurth, K. J. Genestreti, R. M. Skoug, B. A. Larsen, L. M. Kistler, C. Mouikis, and H. Spence (2014), Simulation of Van Allen Probes plasmapause encounters, *J. Geophys. Res. Space Physics*, *119*, 7464–7484, doi:10.1002/2014JA020252.

Green, J. C., T. G. Onsager, T. P. O'Brien, and D. N. Baker (2004), Testing loss mechanisms capable of rapidly depleting relativistic electron flux in the Earth's outer radiation belt, *J. Geophys. Res.*, *109*, A12211, doi:10.1029/2004JA010579.

Hartley, D. P., M. H. Denton, J. C. Green, T. G. Onsager, J. V. Rodriguez, and H. J. Singer (2013), Case studies of the impact of high-speed solar wind streams on the electron radiation belt at geosynchronous orbit: Flux, magnetic field, and phase space density, *J. Geophys. Res. Space Physics*, *118*, 6964–6979, doi:10.1002/2013JA018923.

Horne, R. B., and R. M. Thorne (1993), On the preferred source location for the convective amplification of ion cyclotron waves, *J. Geophys. Res.*, *98*(A6), 9233–9247, doi:10.1029/92JA02972.

Horwitz, J. L., C. R. Baugher, C. R. Chappell, E. G. Shelley, D. T. Young, and R. R. Anderson (1981), ISEE 1 observations of thermal plasma in the vicinity of the plasmasphere during periods of quieting magnetic activity, *J. Geophys. Res.*, *86*(A12), 9989–10,001, doi:10.1029/JA086iA12p09989.

Hu, Y., and R. E. Denton (2009), Two-dimensional hybrid code simulation of electromagnetic ion cyclotron waves in a dipole magnetic field, *J. Geophys. Res.*, *114*, A12217, doi:10.1029/2009JA014570.

Imhof, W. L., H. D. Voss, J. B. Reagan, D. W. Datlowe, E. E. Gaines, J. Mobilia, and D. S. Evans (1986), Relativistic electron and energetic ion precipitation spikes near the plasmapause, *J. Geophys. Res.*, *91*(A3), 3077–3088, doi:10.1029/JA091iA03p03077.

Kletzing, C., et al. (2013), The Electric and Magnetic Field Instrument Suite and Integrated Science (EMFISIS) on RBSP, *Space Sci. Rev.*, *179*(1-4), 127–181, doi:10.1007/s11214-013-9993-6.

Li, Z., R. M. Millan, and M. K. Hudson (2013), Simulation of the energy distribution of relativistic electron precipitation caused by quasi-linear interactions with EMIC waves, *J. Geophys. Res. Space Physics*, *118*, 7576–7583, doi:10.1002/2013JA019163.

Lorentzen, K. R., M. P. McCarthy, G. K. Parks, J. E. Foat, R. M. Millan, D. M. Smith, R. P. Lin, and J. P. Treilhou (2000), Precipitation of relativistic electrons by interaction with electromagnetic ion cyclotron waves, *J. Geophys. Res.*, *105*(A3), 5381–5389, doi:10.1029/1999JA000283.

Loto'aniu, T. M., B. J. Fraser, and C. L. Waters (2005), Propagation of electromagnetic ion cyclotron wave energy in the magnetosphere, *J. Geophys. Res.*, *110*, A07214, doi:10.1029/2004JA010816.

Lyons, L. R., R. M. Thorne, and C. F. Kennel (1971), Electron pitch-angle diffusion driven by oblique whistler-mode turbulence, *J. Plasma Phys.*, *6*, 589–606, doi:10.1017/S0022377800006310.

Mauk, B. H., and N. J. Fox (2010), Electron radiation belts of the solar system, *J. Geophys. Res.*, *115*, A12220, doi:10.1029/2010JA015660.

Millan, R. M., R. P. Lin, D. M. Smith, K. R. Lorentzen, and M. P. McCarthy (2002), X-ray observations of MeV electron precipitation with a balloon-borne germanium spectrometer, *Geophys. Res. Lett.*, *29*(24), 2194, doi:10.1029/2002GL015922.

Millan, R. M., et al. (2013), The Balloon Array for RBSP Relativistic Electron Losses (BARREL), *Space Sci. Rev.*, *179*(1-4), 503–530, doi:10.1007/s11214-013-9971-z.

Miyoshi, Y., K. Sakaguchi, K. Shiokawa, D. Evans, J. Albert, M. Connors, and V. Jordanova (2008), Precipitation of radiation belt electrons by EMIC waves, observed from ground and space, *Geophys. Res. Lett.*, *35*, L23101, doi:10.1029/2008GL035727.

Onsager, T. G., A. A. Chan, Y. Fei, S. R. Elkington, J. C. Green, and H. J. Singer (2004), The radial gradient of relativistic electrons at geosynchronous orbit, *J. Geophys. Res.*, *109*, A05221, doi:10.1029/2003JA010368.

Rodger, C. J., T. Raita, M. A. Clilverd, A. Seppälä, S. Dietrich, N. R. Thomson, and T. Ulich (2008), Observations of relativistic electron precipitation from the radiation belts driven by EMIC waves, *Geophys. Res. Lett.*, *35*, L16106, doi:10.1029/2008GL034804.

Rodriguez, J. V., T. G. Onsager, and J. E. Mazur (2010), The east-west effect in solar proton flux measurements in geostationary orbit: A new GOES capability, *Geophys. Res. Lett.*, *37*, L07109, doi:10.1029/2010GL042531.

Sandanger, M. I., F. Søraas, M. Sørbø, K. Aarsnes, K. Oksavik, and D. Evans (2009), Relativistic electron losses related to EMIC waves during CIR and CME storms, *J. Atmos. Sol. Terr. Phys.*, *71*(10-11), 1126–1144, doi:10.1016/j.jastp.2008.07.006.

Spasojević, M., H. U. Frey, M. F. Thomsen, S. A. Fuselier, S. P. Gary, B. R. Sandel, and U. S. Inan (2004), The link between a detached subauroral proton arc and a plasmaspheric plume, *Geophys. Res. Lett.*, *31*, L04803, doi:10.1029/2003GL018389.

Spence, H., et al. (2013), Science goals and overview of the Radiation Belt Storm Probes (RBSP) Energetic Particle, Composition, and Thermal Plasma (ECT) suite on NASA's Van Allen Probes mission, *Space Sci. Rev.*, *179*(1-4), 311–336, doi:10.1007/s11214-013-0007-5.

Summers, D., and R. M. Thorne (2003), Relativistic electron pitch-angle scattering by electromagnetic ion cyclotron waves during geomagnetic storms, *J. Geophys. Res.*, *108*(A4), 1143, doi:10.1029/2002JA009489.

Summers, D., B. Ni, and N. P. Meredith (2007), Timescales for radiation belt electron acceleration and loss due to resonant wave-particle interactions: 1. Theory, *J. Geophys. Res.*, *112*, A04206, doi:10.1029/2006JA011801.

Takahashi, K., S. Ohtani, R. E. Denton, W. J. Hughes, and R. R. Anderson (2008), Ion composition in the plasma trough and plasma plume derived from a combined release and radiation effects satellite magnetoseismic study, *J. Geophys. Res.*, *113*, A12203, doi:10.1029/2008JA013248.

Thorne, R. M., and L. J. Andreoli (1981), Mechanisms for intense relativistic electron precipitation, in *Exploration of the Polar Upper Atmosphere*, edited by R. M. Thorne and L. J. Andreoli, pp. 381–394, Springer, Dordrecht, Netherlands, doi:10.1007/978-94-009-8417-2.

Thorne, R. M., and C. F. Kennel (1971), Relativistic electron precipitation during magnetic storm main phase, *J. Geophys. Res.*, *76*(19), 4446–4453, doi:10.1029/JA076i019p04446.

Thorne, R. M., R. B. Horne, V. K. Jordanova, J. Bortnik, and S. Glauert (2006), *Magnetospheric ULF Waves: Synthesis and New Directions, Geophys. Monogr. Ser.*, vol. 169, pp. 213–223, AGU, Washington, D. C., doi:10.1029/GM169.

Tsyganenko, N. (1989), A magnetospheric magnetic field model with a warped tail current sheet, *Planet. Space Sci.*, *37*(1), 5–20, doi:10.1016/0032-0633(89)90066-4.

Usanova, M. E., F. Darrouzet, I. R. Mann, and J. Bortnik (2013), Statistical analysis of EMIC waves in plasmaspheric plumes from Cluster observations, *J. Geophys. Res. Space Physics*, *118*, 4946–4951, doi:10.1002/jgra.50464.

Vampola, A. L. (1971), Electron pitch angle scattering in the outer zone during magnetically disturbed times, *J. Geophys. Res.*, *76*(19), 4685–4688, doi:10.1029/JA076i019p04685.

Weaver, C. E., M. R. Lessard, M. J. Engebretson, R. M. Millan, A. J. Halford, R. B. Horne, H. J. Singer, J. C. Green, and M. E. Usanova (2013), Ground and satellite EMIC wave observations in conjunction with BARREL electron precipitation. AGU, Fall Meeting 2013, abstract No. SM23C-07.

West, H. I., R. M. Buck, and J. R. Walton (1973), Electron pitch angle distributions throughout the magnetosphere as observed on Ogo 5, *J. Geophys. Res.*, *78*(7), 1064–1081, doi:10.1029/JA078i007p01064.

Wygant, J., et al. (2013), The electric field and waves instruments on the radiation belt storm probes mission, *Space Sci. Rev.*, *179*(1-4), 183–220, doi:10.1007/s11214-013-0013-7.

Yahnin, A., and T. Yahnina (2007), Energetic proton precipitation related to ion-cyclotron waves, *J. Atmos. Sol. Terr. Phys.*, *69*(14), 1690–1706, doi:10.1016/j.jastp.2007.02.010.

Young, D. T., J. Geiss, H. Balsiger, P. Eberhardt, A. Ghielmetti, and H. Rosenbauer (1977), Discovery of He^{2+} and O^{2+} ions of terrestrial origin in the outer magnetosphere, *Geophys. Res. Lett.*, *4*(12), 561–564, doi:10.1029/GL004i012p00561.